December 23, 2007

**E94-010 Analysis Note**

# Draft

K. Slifer[†]
*University of Virginia*
*slifer@jlab.org*

We present here details of the final analysis of JLab Experiment 94-010.

**Contents**



[†]Previously Temple University

## 1 Introduction

In order to reduce systematic errors and clarify some outstanding issues, we have performed a complete reanalysis of the $^3$He data of experiment E94-010. A secondary goal of this endeavor was to properly document and archive the analysis tools and data. This note details any changes from the previous results, and documents some analysis steps that were not previously made explicit.

## 2 Unpolarized $^3$He Raw Cross Sections

The unpolarized experimental cross section is given by:

$$\sigma_{raw} = \left(\frac{d\sigma}{dE' d\Omega}\right)_{raw} = \frac{N_f^*}{N_i \rho} \times \frac{1}{\Delta Z \Delta\Omega \Delta E'} \tag{1}$$

Where $N_f^*$ is the number of scattered electrons detected, corrected for detector and software efficiencies, prescalers and for deadtime. $N_i$ is the number of incident electrons. $\rho$ is the (number) density of the target. $\Delta Z$ is the length of the target seen by the spectrometer. $\Delta E'$ is the energy binning of the scattered electrons. And $\Delta\Omega$ is the angular acceptance.

In practice, we use a montecarlo technique to determine the product $\Delta Z \Delta\Omega \Delta E'$ as described in Sec. 8.1 of Ref. [1]. Explicitly, the raw cross section for HRS-L is given by:

$$\sigma_{raw} = \frac{P_1 N_{T_1} + P_2 N_{T_2}}{\epsilon(L.T.)\frac{Q}{e}\rho} \left(\frac{N_{MC}^{in}}{N_{MC}} \frac{1}{\Delta Z_{MC} \Delta\Omega_{MC} \Delta E'_{MC}}\right) \tag{2}$$

Here $\epsilon$ is the detector efficiency, L.T. is the DAQ livetime, Q represents the charge, and $e = 1.6 \cdot 10^{-19}$ C. $\rho$ is the target density in Amagats. $N_{MC}^{in}$ is the number of generated montecarlo events, $N_{MC}$ is the number of montecarlo events that pass through the acceptance and all software cuts. $N_{T_1}$ ($N_{T_2}$) are the number of detected electrons that pass all cuts and have good (bad) scintillator signal. And $P_1$ ($P_2$) is the $T_1$ ($T_2$) prescaler. The cross section for HRS-R is given by the same expression, but with the 1(2) subscripts replaced with 3(4).

Propagation of statistical errors reveals that:

$$d\sigma = \frac{1}{\epsilon(L.T.)\frac{Q}{e}\rho N_{MC}} \cdot \sqrt{\left[P_1^2 N_{T_1}\left(1 + \left(N_{T_1}\frac{dN_{MC}}{N_{MC}}\right)^2 + P_2^2 N_{T_2}\left(1 + \left(N_{T_2}\frac{dN_{MC}}{N_{MC}}\right)^2\right)\right)\right]}$$

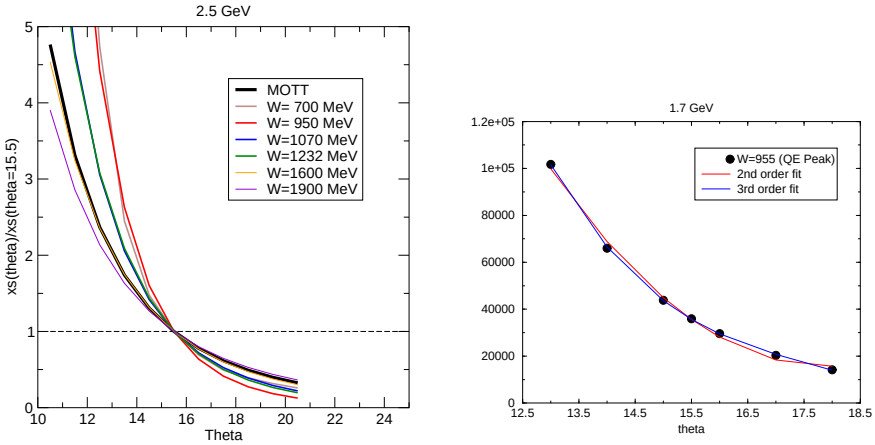


Figure 1: **Left:** Angular dependence of the cross section for the model at various values of missing mass W, compared to the Mott variation. **Right:** Interpolation of the model's angular dependence to intermediate angles for W=955 MeV. The $2^{nd}$-order fit was used, but it can be seen that there is little variation if a higher order interpolation is used.

Notice that in the limit of no scintillator inefficiency, and infinite MC events, the uncertainty expression simplifies to the more familiar:

$$\lim_{N_{T_2}, dN_{MC} \to 0} \left( \frac{d\sigma}{\sigma} \right) = \frac{1}{\sqrt{N_{T_1}}} \tag{3}$$

### *2.1 Finite Acceptance and Bin-centering Correction*

In order to account for the fact that the spectrometer acceptance and analysis cuts allow for a spread of angular distributions, we normalize the data to the value at the central angle. We also correct each event to the central value of it's respective $\nu$-bin.

For each event with a given kinematic pair $(\nu, \theta)$, we calculate a model[‡] radiated cross section at $(\nu, \theta)$ and $(\nu_0, \theta_0)$. Then each event is weighted by the factor $\sigma(\theta_0, \nu_0)/\sigma(\theta, \nu)$. Here, $\theta_0 \approx 15.5^\circ$ and $\nu_0$ is the central value of the particular $\nu$-bin that the event falls into. Radiating the model for each ntuple event is not feasible, given the number of events recorded. Instead, a table of

[‡]QFS scaled to reproduce the raw data to within a few percent. Note that we made the approximation in the model that the target was pure $^3$He, and only considered inelastic radiative effects.

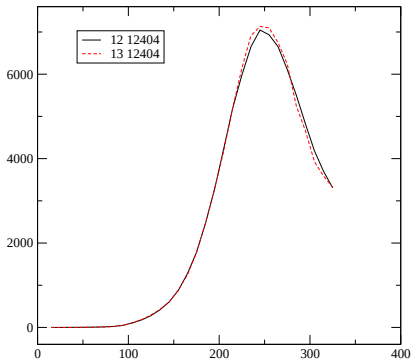


Figure 2: Finite acceptence corrected cross section compared with data from Cut 13. Cut 13 has a very restricted angular range so the finite acceptance correction is very small. The good agreement of these two spectra shows that the finite acceptance correction is being applied correctly.

radiated cross sections were generated in the range $13^\circ < \theta < 18^\circ$. Then these tables are interpolated to the desired $(\nu, \theta)$ value.

We mention here that the Mott cross section is not a good weighting factor for $W < 1600$ MeV, since the angular dependence is quite different from the resonance data as shown in Fig. 1. For larger values of W, Mott weighting is not a bad approximation.

Of the two above-mentioned corrections, the $\theta$-centering dominates. We binned the data in 1, 10, or 50 MeV intervals, depending on the measured statistical error. The $\nu$-bin centering correction was found to be significant only for the 50 MeV binned data. As discussed in section 2.2, we tested several different acceptance cuts and their systematic effect on the cross section. Applying the centering corrections improved the agreement among all cuts dramatically. Figs. 3 to 5 show the size of the corrections to the cross section. The top panel of each plot shows the unpolarized cross section for reference.

Since we apply this correction factor regardless of the helicity of the event, the correction is also automatically carried through to the asymmetries. This is discussed in section 5.3.

We estimate the uncertainty of the correction by comparing the corrected data to data formed with an extremely tight cut on scattering angle (cut 13 of Table 1). See Fig. 2. The difference is typically less then 2%, and is displayed in Table 2. Note that from hereon, we make no distintion between the $\nu-$centering and $\theta$-centering correction and refer to them collectively as the "Finite Acceptance Correction".

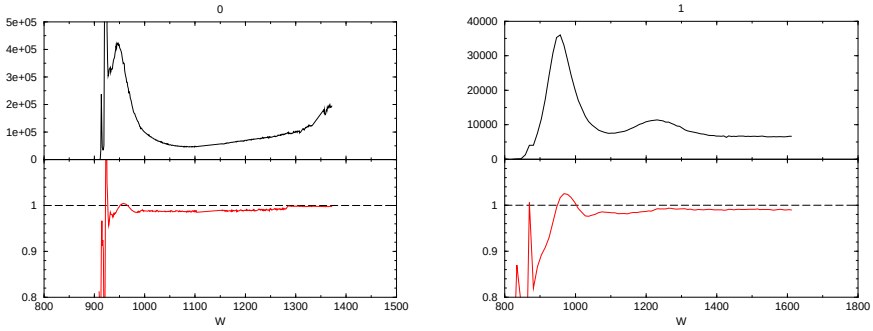


Figure 3: **Top:** XS. **Bottom:** Finite acceptance correction. **Left:**0.8 GeV **Right:**1.7 GeV

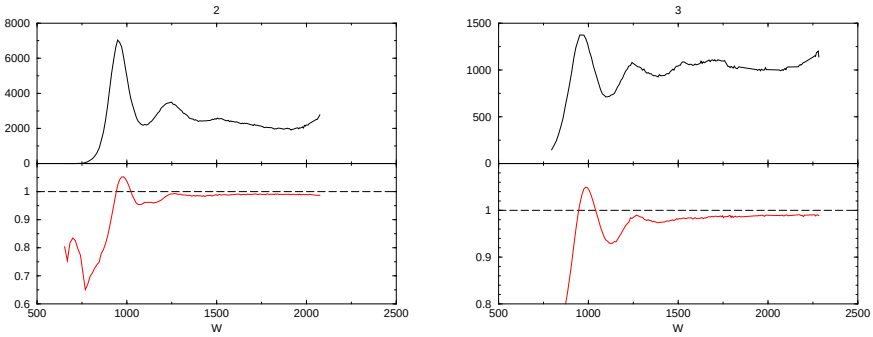


Figure 4: **Top:** XS. **Bottom:** Finite acceptance correction. **Left:**2.5 GeV **Right:**3.4 GeV

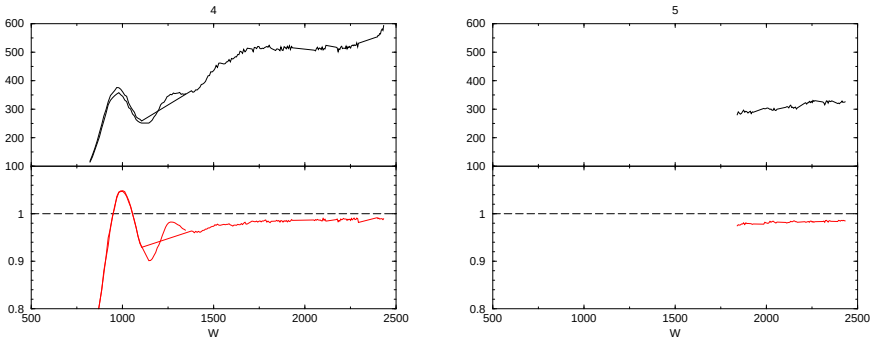


Figure 5: **Top:** XS. **Bottom:** Finite acceptance correction. **Left:**4.3 GeV **Right:**5.1 GeV

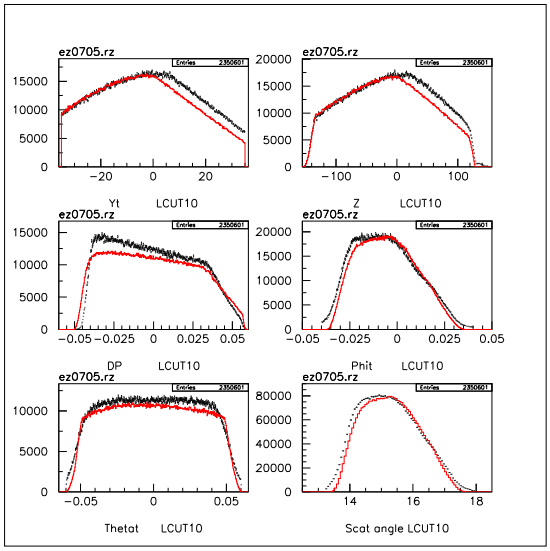


Figure 6: Cut 10. Comparison of data (black) and M.C. (red).

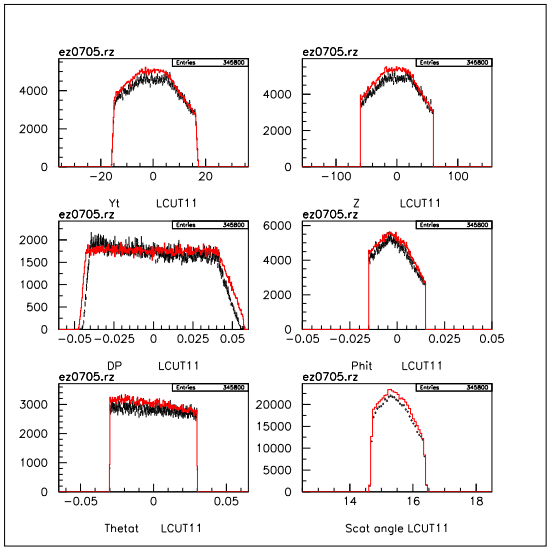


Figure 7: Cut 11. Comparison of data (black) and M.C. (red).

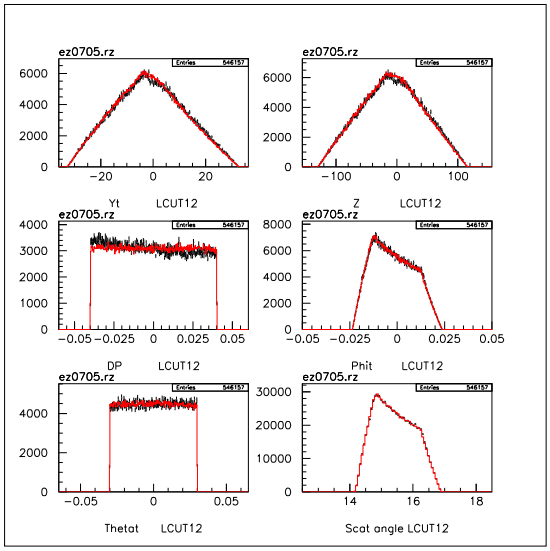


Figure 8: Cut 12. Comparison of data (black) and M.C. (red).

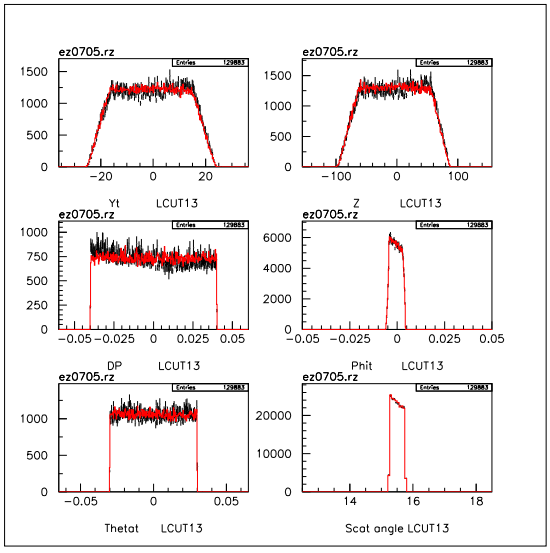


Figure 9: Cut 13. Comparison of data (black) and M.C. (red).

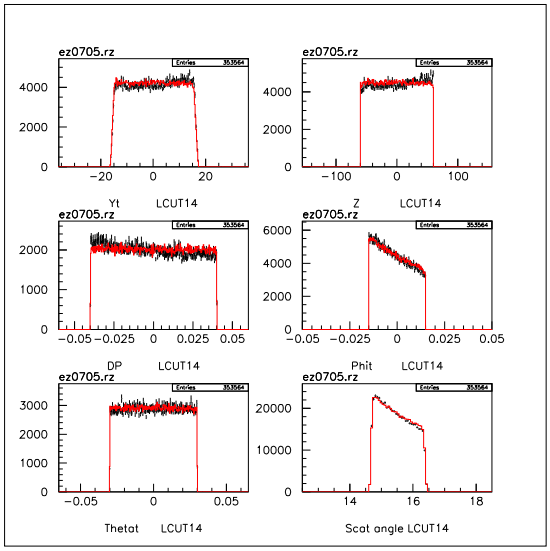


Figure 10: Cut 14. Comparison of data (black) and M.C. (red).

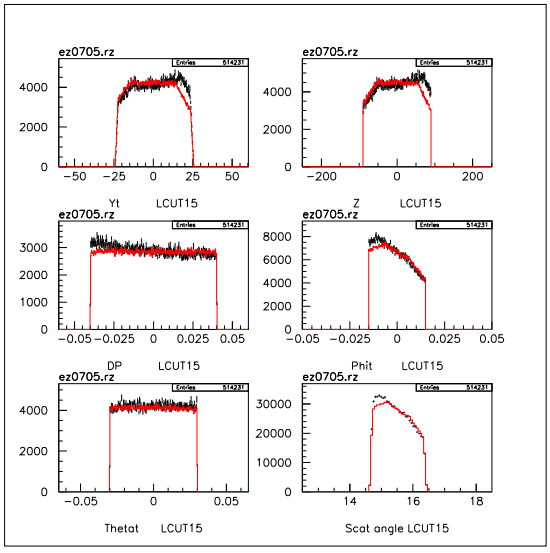


Figure 11: Cut 15. Comparison of data (black) and M.C. (red).

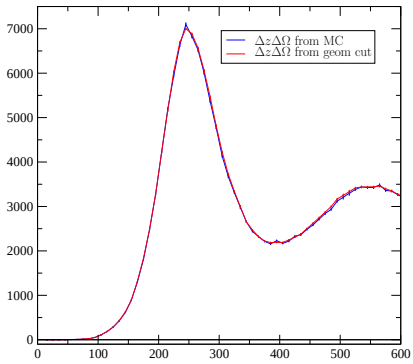


Figure 12: The cross section formed using the montecarlo to determine $\Delta z \Delta\Omega$ compared to the same cross section with geometrically defined $\Delta z \Delta\Omega$ for LCUT 14. The agreement is better than 1%. Note that this does not hold when a longer target length is used, as in LCUT 15.

### *2.2 Acceptance Cuts*

To quantify our knowledge of the spectrometer acceptence we tested several different cuts as detailed in Ref [1]. For this updated analysis, we tested many new cut configurations, finally settling on an optimized cut to maximize statistics and improve agreement between montecarlo and data. A small subset of the new cuts are shown in Table 1. Note that cut 10 and 11 are identical to cuts 10 and 13 of Ref. [1], and were the cuts used to generate the previous published asymmetries and cross sections respectively. Details of these cuts are in Ref. [1]. We refer to them simply as *Big Box* and *Small Box*.

| Cut | Description | $N/N_0$ |
|---|---|---|
| 10 | Big Box | 6.8 |
| 11 | Small Box | 1.0 |
| 12 | NL | 1.6 |
| 13 | NL + $15.25 < \theta < 15.75$ | 0.4 |
| 14 | Small Box ($\|z\| < 6$) | 1.0 |
| 15 | Small Box ($\|z\| < 9$) | 1.5 |

Table 1: Acceptance cuts. Note that cut 10 and 11 are identical to cuts 10 and 13 of the previous ananalysis, and were the cuts used to generate the previous published asymmetries and cross sections respectively. $N/N_0$ refers to the ratio of events that pass the cut compared to the previous cross section cut.

A new optimized cut, which we label the *NL*-cut, since Nilanga Liyanage advocated something quite similar in Ref. [2] is:

$$\begin{aligned} |\phi_T + y_T| &< 0.025 \\ |\phi_T - 0.375 y_T| &< 0.025 \\ |\Delta\theta| &< 0.030 \\ |\Delta P| &< 0.040 \\ |\theta - \theta_0| &< 2.5^\circ \end{aligned}$$

As shown in Fig. 8, this cut improves our agreement with the montecarlo considerably compared to the previous cut (Fig. 7). It also improves the statistical error as shown in Table 1. To complete our set of cuts we tested a pure small box cut with a target length of 12 and 18 cm respectively.

Comparison of all cuts to the montecarlo are shown in Figs. 6 to 11. For the final analysis we utilize LCUT 10 with finite acceptance correction applied for the asymmetry, and LCUT 13 with no finite acceptance correction for the unpolarized cross section. The loss of statistics for the unpolarized cross section is not significant because the final statistical error is dominated by the asymmetry.

### $\phi_t$ Shift

We note here that several previous analyses of E94-010 data advocated applying an ad-hoc shift of 3 mrad to the $\phi_{targ}$ variable in order to improve agreement between the data and monte-carlo simulation. We did properly account for all spectrometer mispointing, but we found no need for any further shift. We note that there does appear to be an offset noticible in the loose cut 10 (Fig. 6), but that this vanishes when any reasonable cut is made on the acceptance.

## 3 Raw Cross Section Systematics

The systematic uncertainty varies as a function of scattered electron energy. To provide global values of the systematic we take the bin by bin values and average them via:

$$\Delta^2 = \frac{\sum\limits_i \frac{1}{\omega^2} \left( \frac{\sigma_i - \tilde{\sigma}_i}{\tilde{\sigma}_i} \right)^2}{\sum\limits_i \frac{1}{\omega^2}} \tag{4}$$

where $\tilde{\sigma}$ is some reference *good* cross section. This helps to eliminate any statistical influence on the systematic by averaging over many bins. $\omega$ is the chosen weighting of each point. Since the statistical error is nearly constant as a function of $\nu$ for each spectrum, we set $\omega = 1$.

The results of this study are shown in Table 2. The systematic uncertainty is in general smaller than the previous analysis (for which we assumed a uniform 5%). This is mostly due to reduction of the $\Delta\Omega\Delta z$ uncertainty. However, there are two new contributions which we previously overlooked: the finite acceptance correction error, and the normalization error for the 0.8 and 4.3 GeV quasielastic data.

Table 3 shows the raw cross section spectrometer difference. Since this is before radiative corrections, some disagreement is expected due to the nonequal radiation lengths encountered. As such, this value represents an overestimate of the maximum systematic uncertainty.

Even so, we can learn quite a bit by comparing the raw spectrometer cross sections as shown in figs. 16 to 18. A strong crossover occurs with 1.7 and 3.0 GeV for the cell Armegeddon. This cell had very different left/right thicknesses and is the only GE180 cell as detailed in Table 4. All other cells are Corning 1720. There was no direct measurement of Armegeddon thicknesses either. The radiation lengths come entirely from elastic analysis [4]. With the exception of Armeggedon and 862 MeV, the cross sections agree to 5%. We can see from figs. 19 to 21 that this behaviour is inconsistent with an offset in scattering angle or an error in knowledge of the material thickness before scattering, but is entirely consistent with an error in the value for material thickness after scattering.

The $T_4$ correction was corrupted for the 5 GeV HRS-R data, so the HRS-R arm xs data should be discarded. Nevertheless, the two arms still agree to 5.2%.

### *3.1 $\Delta z\Delta\Omega$ Uncertainty*

Our previous analysis relied on a monte carlo technique to determine the factor $\Delta z\Delta\Omega$ when constructing the cross sections as detailed in Ref. [1]. To determine the systematic uncertainty of this technique we examined several alternate acceptance cuts to determine how sensitive the cross section was to this input. We now believe this to be an overestimate of the uncertainty. Instead we have determined the factor $\Delta z\Delta\Omega$ via two methods. First, by the standard montecarlo technique, and second by simply using the geometrically defined value of $\Delta z\Delta\Omega$ in LCUT 14. The cross section with $\Delta z\Delta\Omega$ from the MC typically agrees with the cross section from a geometrically defined acceptance

| $\mathbf{E_0}$**(GeV)** | | **0.8** | **1.7** | **2.5** | **3.3** | **4.3** | **5.1** |
|---|---|---|---|---|---|---|---|
| Target density | | | | 2.9 | | | |
| Det. eff: Scintillator | | | | 1.0 | | | |
| Det. eff: VDC | | | | 1.0 | | | |
| Charge | | | | 1.0 | | | |
| PID eff (cut & detection) | | | | 0.5 | | | |
| Energy | | | | 0.5 | | | |
| $\Delta\Omega\Delta z$ | (QE) | 1.4 | 0.6 | 1.6 | 1.1 | 1.1 | — |
| Finite Acceptace Corr. | (QE) | 2.2 | 1.4 | 3.0 | 3.0 | 4.1 | — |
| Normalization | (QE) | 5.0 | — | — | — | 5.0 | — |
| $\Delta\Omega\Delta z$ | (Inel) | 1.4 | 2.2 | 0.8 | 0.8 | 1.0 | 1.2 |
| Finite Acceptance Corr. | (Inel) | 2.2 | 1.0 | 1.2 | 1.4 | 1.9 | 1.9 |
| Normalization | (Inel) | — | — | — | — | — | — |
| **Total Quasielastic** | | **6.6** | **3.7** | **4.8** | **4.7** | **7.4** | — |
| **Total Inelastic** | | **4.3** | **4.2** | **3.7** | **3.8** | **4.1** | **4.1** |

Table 2: Raw cross section systematics in percent for $W \leq 1073$ MeV (QE), and for $W > 1073$ MeV (Inel). Our previous analyses assumed a uniform 5% throughout.

| $\mathbf{E_0}$**(GeV)** | | **0.8** | **1.7** | **2.5** | **3.3** | **4.3** | **5.1** |
|---|---|---|---|---|---|---|---|
| Spectrometer difference | (QE) | 8.5 | 7.9 | 3.7 | 10.4 | — | — |
| Spectrometer difference | (Inel) | 11.6 | 6.5 | 4.1 | 3.9 | 4.9 | $5.2^{\dagger}$ |

Table 3: Raw cross section spectrometer difference: the average difference (in percent) in the unpolarized cross section for each energy, in the quasielastic and inelastic regions. $^{\dagger}$: The $T_4$ correction was corrupted for the 5 GeV HRS-R data, so this data should in principle be discarded. Nevertheless, the two arms still agree to 5.2%.

at the 1% level for this cut, and we reduce the systematic accordingly. See Fig. 12 and Table 2. We note that this method fails when the target length is increased as in LCUT 15.

### *3.2 PID uncertainty*

Previously we assumed an uncertainty of 1% relative for all kinematics arising from the particle identification detection efficiency, and an additional 1% relative arising from the exclusion of good events due to the PID cuts. This was an overestimate. E94-010 had excellent PID detector efficiency, and the PID cuts were chosen specifically so that they never excluded more than 1% of good events. For the present analysis we assign a total PID systematic of 0.5%. We

tested this by comparing the unpolarized cross section formed with Cerenkov cut only to the cross section formed with both Cerenkov and calorimeter cuts[§]. In the absolute worst case these two cross sections agreed to within 0.5%.

### *3.3 Renormalization*

We have two independent momentum settings which cover well the 0.8 GeV quasi-elastic cross section as shown in Fig. 13. The value of the cross section at the QE peak differs by approximately 5% from these two momentum settings so we include an additional "normalization" uncertainty of 5% for this spectra. To be clear, no normalization is applied, the two statistically weighted spectra have simply been combined.

We have a similar situation for the 4 GeV quasi-elastic data as shown in Fig. 14. Here, the two independent measurements come from two different target cells. Since the material thickness of the two cells is nearly identical, the difference most likely arises from the assumed density. In figure 14, we note that the density of cell Nephali is the outlier of all E94010 cells. In light of this, it is more likely that the density of Nephali is overestimated than Sysiphos underestimated. Because of this, we scale the Nephali data to match the Sysiphos data (5% difference) and assign a 5% normalization uncertainty. Fig. 13 (right panel) shows similar behavior for the Right arm spectrometer cross section result.

### *3.4 Other Systematics*

As detailed in Appendix F of Ref. [1], the 0.8 GeV data contains three spectrometer settings at large energy loss ($\nu > 450$ MeV) for which the HRS-L dipole momentum was not matched to the quadrupoles' magnetic setting. To limit the effect of this mismatch, we cut aggressively on the central acceptance region in order to minimize the need for the focusing that is normally provided by the quadrupoles. Accordingly the statistical error was inflated artificially by a factor of 5 and the systematic error was inflated by a factor of 3 for $\nu \geq 422$ MeV.

[§]We performed this test in a region of moderate pion contamination. When the pion contamination is large these two results differ strongly of course, because the full PID cut is needed.

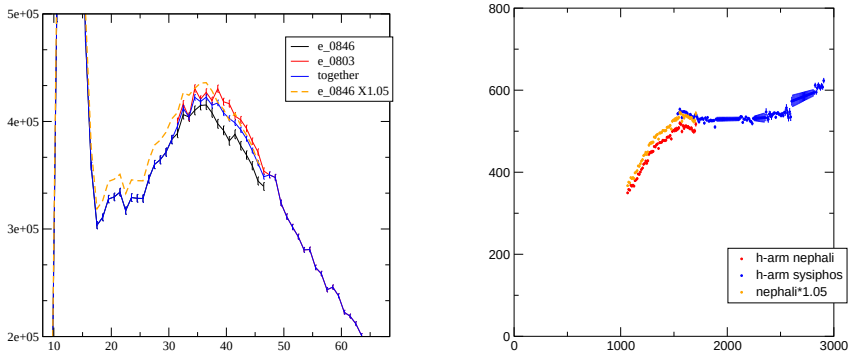


Figure 13: **Left:** 862 MeV QE data. Disagreement is found between the two spectrometer settings which registered quasielastic data. **Right:** Renormalization of the 4 GeV QE Nephali data. HRS-R.

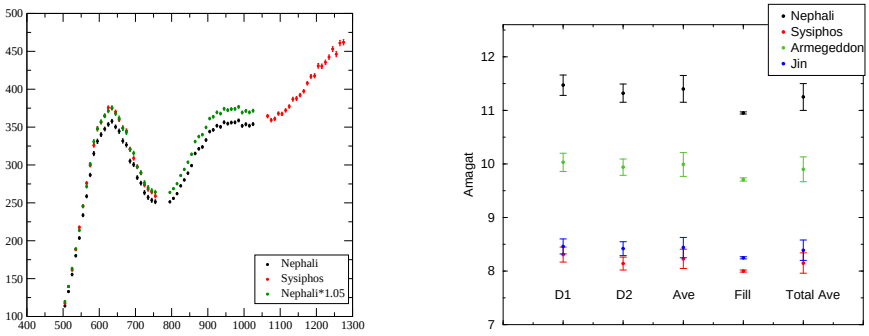


Figure 14: Renormalization of the 4 GeV QE Nephali data. **Left:** QE cross section from two different target cells. **Right:** Density of all E94010 target cells.

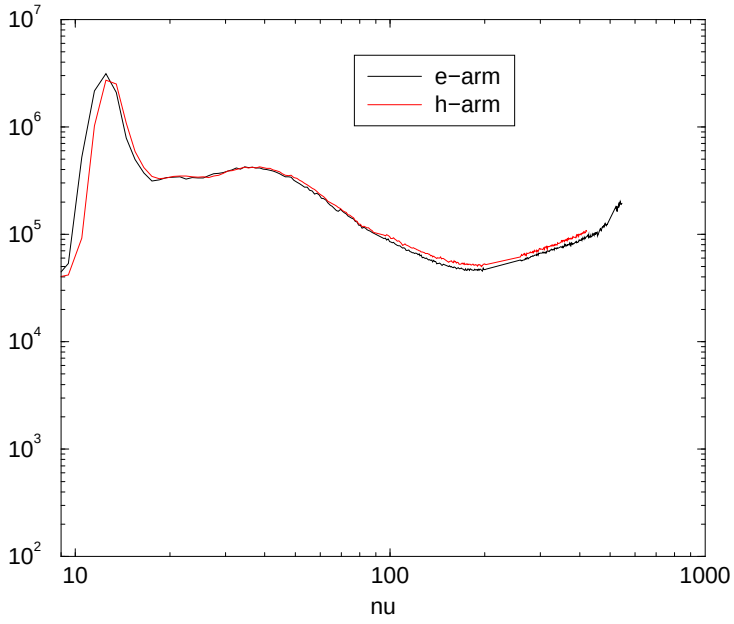


Figure 15: Comparison of HRS-L and HRS-R xs. The observed cross-over is consistent with a larger $T_a$ encountered by the electrons in the HRS-R.

| E0 | Cell | Glass | Tb | $\text{Ta}_{Left}$ | $\text{Ta}_{Right}$ | L/R Diff.(%) |
|---|---|---|---|---|---|---|
| 0.8 | Sysiphos | C1720 | 7.184E-3 | 4.166E-2 | 4.27E-2 | 2.5 |
| 1.7 | Armegeddon | **GE180** | 7.922E-3 | 7.492E-2 | 8.505E-2 | **13.5** |
| 2.5 | Jin | C1720 | 7.269E-3 | 3.739E-2 | 3.902E-2 | 4.3 |
| 3.3 | Armegeddon | **GE180** | 7.922E-3 | 7.492E-2 | 8.505E-2 | **13.5** |
| 4.3 | Sysiphos | C1720 | 7.184E-3 | 4.166E-2 | 4.273E-2 | 2.5 |
| 4.3 | Nephali | C1720 | 7.381E-3 | 4.116E-2 | 4.116E-2 | 0.0 |
| 5.0 | Jin | C1720 | 7.269E-3 | 3.739E-2 | 3.902E-2 | 4.3 |

Table 4: Radiation lengths before (Tb) and after (Ta) the cell for each target used in E94-010. The largest difference in material thickness after scattering for left/right spectrometer is found for cell *Armegeddon*, the only GE180 cell. Note that the R.L. values for *Armegeddon* were determined indirectly via the elastic scattering analysis.

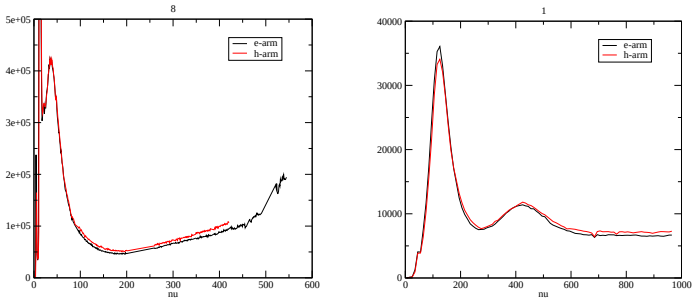


Figure 16: Comparison of Left/Right Spectrometer.**Left:**0.8 GeV **Right:**1.7 GeV

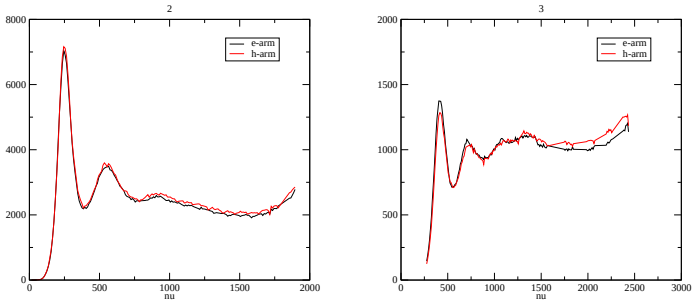


Figure 17: Comparison of Left/Right Spectrometer.**Left:**2.5 GeV **Right:**3.4 GeV

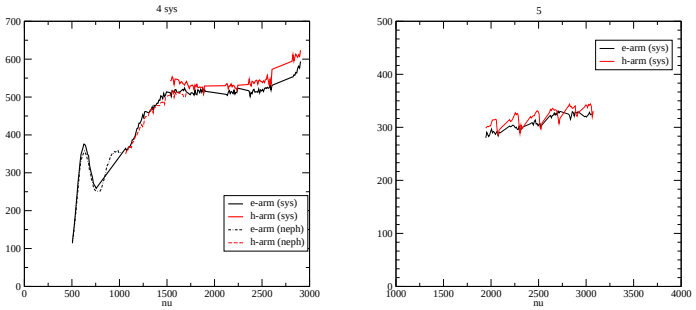


Figure 18: Comparison of Left/Right Spectrometer.**Left:**4.3 GeV **Right:**5.1 GeV

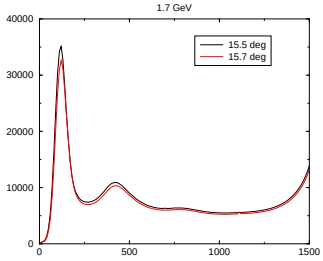


Figure 19: Model generated spectra at two slightly different angles.

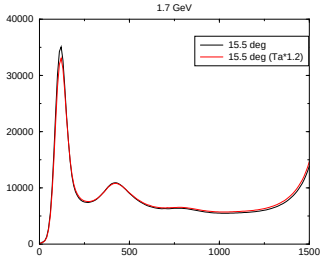


Figure 20: Model generated spectra with 20% variation of pre-target material thickness.

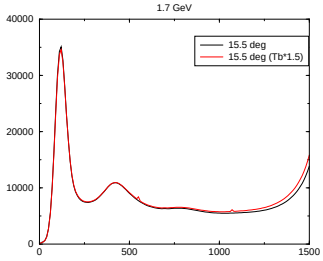


Figure 21: Model generated spectra with 20% variation of post-target material thickness.

## 4 Radiative Corrections

### *4.1 Elastic Tail Subtraction*

We have at our disposal two methods for determining the $^3$He elastic tail contamination of our data. The first is the legacy SLAC code *Rosetail* modified for our purposes as described in Ref.[3]. In this code the elastic peak is treated as a delta function, and the detector resolution and Fermi broadening are ignored. Radiative corrections follow the full treatment of Mo and Tsai [5] or Akusevich and Sumenko [6] for unpolarized and polarized scattering respectively. The second code is the E94010 Monte Carlo as implemented by A. Deur [4], which does include resolution effects, but treats radiative corrections in a simplified manner.

In the quasielastic region, radiative effects are small and in fact can be treated as a constant multiplicative ($\nu$-dependent) factor in first order. Here the dominant effect is the resolution (the delta function approximation fails) and the treatment of A. Deur's M.C. is most appropriate. At larger $\nu$, radiative effects dominate and the SLAC based code should be used.

Disagreement between *Rosetail* and the Montecarlo radiated tail is at the 20% level at large $\nu$. Since the Montecarlo is able to reproduce the data quite well at the elastic peak (as shown in Figs. 22 and 23), we assign 10% error on elastic tail subtraction near the peak ($\nu \leq 50[100]$ MeV for 0.8 [1.7] GeV respectively) and 20% at higher nu. For the other energies 20% uncertainty is assumed for all $\nu$. In practice, this has no real impact due to the smallness of the elastic tail contribution for these energies. We also assign 20% error to the nitrogen elastic tail subtraction which again has negligible impact on the final results. The nitrogen dilution contribution is assumed known at the 7-52% level as described in [3]. In general, the uncertainty is larger at lower $Q^2$. It is generated from QFS tuned to match the limited E94010 nitrogen reference cell data. The uncertainty for the lowest two energies could of course be reduced with a more careful study which might reveal why the two codes disagree at larger $\nu$. We note that the Rosetail code has been tested against the classic results of Mo and Tsai and reproduces the published results quite well as displayed in Fig. 25. So the most likely scenario is that the MC results are unreliable at large $\nu$ and we are overestimating the tail subtraction error in this region.

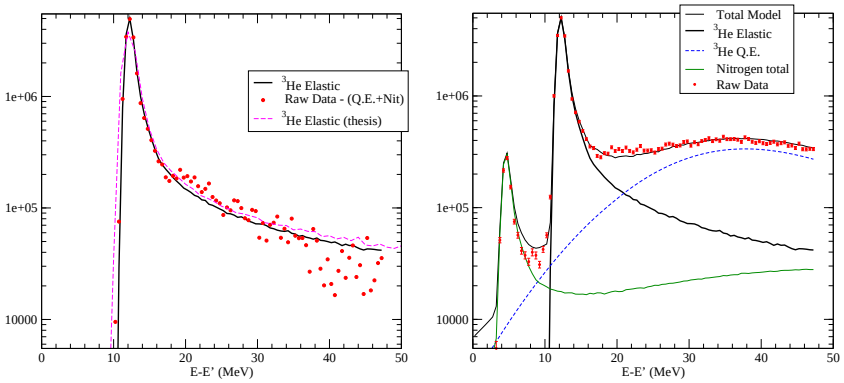


Figure 22: 862 MeV. **Left:** After subtracting out the model estimates of Nitrogen (elastic+inelastic) and $^3$He quasielastic, the Montecarlo generated $^3$He elastic peak is fitted to the data. Our previous analysis result is shown with dotted line. **Right:**Comparison of the raw measured cross section to the model, which contains contributions from the $^3$He and Nitrogen elastic tails, and the $^3$He and Nitrogen inelastic.

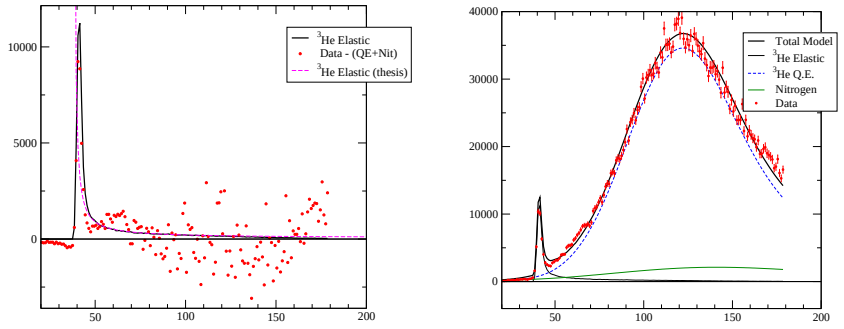


Figure 23: 1716.9 MeV. **Left:** After subtracting out the model estimates of Nitrogen (elastic+inelastic) and $^3$He quasielastic, the Montecarlo generated $^3$He elastic peak is fitted to the data. Our previous result is shown with dotted line. **Right:** Comparison of the raw measured cross section to the model, which contains contributions from the $^3$He and Nitrogen elastic tails, and the $^3$He and Nitrogen inelastic.

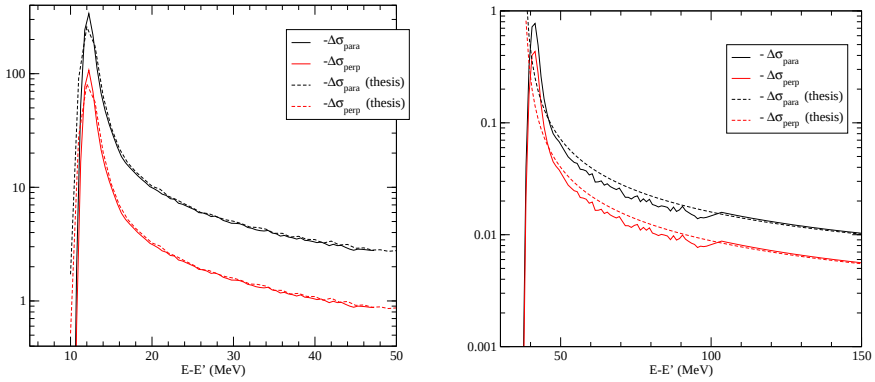


Figure 24: Plot of the polarized elastic tails. **Left:** 862 MeV. **Right:** 1716.9 MeV. The unpolarized elastic peak normalization factor is used to normalize the polarized elastic peaks also. Dotted lines shows previous results. Note that the sign of the polarized peaks have been reversed to allow use of log scale. The discontinuity represents the joining of the MC and Rosetail results.

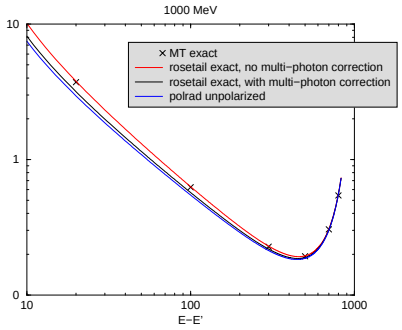


Figure 25: Comparison of Rosetail unpolarized elastic proton tail to the published results of Mo and Tsai at 1.0 GeV.

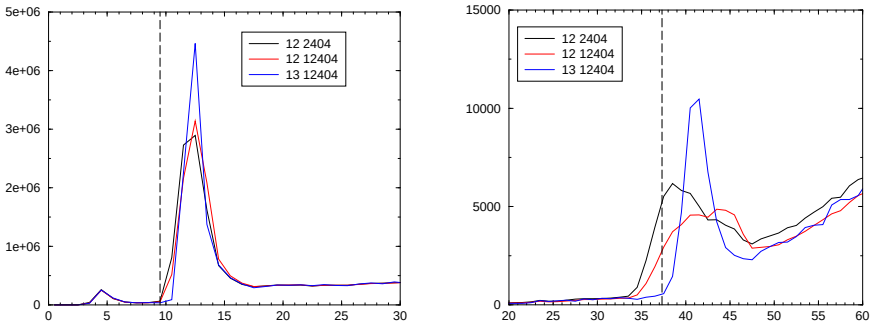


Figure 26: **Left:** 0.8 GeV Elastic Peak. The elastic peak appears in the data at approximately $\nu = 12.4$ MeV, displaced from what the prediction of Eq. 5, shown with dotted line. **Right** Similar, but for 1.7 GeV

### *4.2 Ionization Loss*

Kinematic restraints require the following relation for elastic scattering:

$$E' = \frac{E_0}{1 + E/M(1 - \cos\theta)} \tag{5}$$

Fig. 26 reveals a shift from the expected elastic peak position. Assuming that we know the incident energy and scattering angle accurately[¶], we may use this to determine the ionization loss of the scattered electrons. Previously, we observed that the predicted loss [7] could not fully explain the observed shifts in the data and instead determined the ionization loss by matching the montecarlo generated elastic tail to the falling edge of the data elastic tail. This implied a value of $\Delta = 1.5$ MeV. The new analysis implies

$$\Delta = 2.9 \pm 0.5 \ \text{ MeV, for } E_0 = 0.8 \text{ GeV} \tag{6}$$

$$\Delta = 3.8 \pm 0.5 \ \text{ MeV, for } E_0 = 1.7 \text{ GeV} \tag{7}$$

Note that by matching the elastic data to the expectation, we also ensure that the spectrometer constant is correct.

[¶]One of the assumed values for energy or scattering angle would need to be incorrect by an unexplainable 14% to otherwise explain the observed shift.

### *4.3 Inelastic Radiative correcitons to the Unpolarized Cross sections*

We assume 5% uncertainty on the inelastic radiative corrections except for the lowest energy where we assume 15%.

## 5 Asymmetries

$T_2$ ($T_4$) events represent otherwise good events that failed to trigger one of the scintillators in the e-arm (h-arm). Over the course of the run, the scintillator efficiency gradually deteriorated, until these events represented as much as 13% of the recorded events. They were typically heavily prescaled which makes it disadvantageous to utilize them when forming the asymmetry, since they increase the statistical and systematic error considerably. We exclude them from the asymmetries, implicitly assuming that the scintillator efficiency is helicity-independent.

### *5.1 Systematic Error*

The systematic error of the asymmetries is dominated by the polarimetry. We assume and uncertainty of 4% for the target polarization and 3% for the beam polarization leading to a total uncertainty of 5%. This is unchanged from our previous analysis.

### *5.2 Statistical Error*

The asymmetry is formed as:

$$A = \frac{1}{P_B P_T} \frac{N_- - N_+}{N_- - N_+} \tag{8}$$

where

$$N_\pm = \frac{Pre}{1 - DT_\pm} \frac{N_\pm^{raw}}{Q_\pm} \tag{9}$$

Note that we do not directly correct for the dilution $f$ since the asymmetry is directly multiplied by the unpolarized cross section and in the product the dilution cancels.

The statistical error is given by:

$$dA = \frac{1}{P_B P_T} \frac{2}{(N_+ + N_-)^2} \sqrt{(N_- \delta N_+)^2 + (N_+ \delta N_-)^2} \tag{10}$$

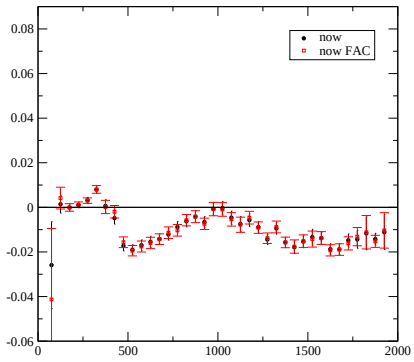


Figure 27: Finite acceptence correction effect on Asymmetry.

where

$$\delta N_{\pm} = \frac{Pre}{(1 - DT_{\pm})} \frac{1}{Q_{\pm}} \sqrt{N_{\pm}^{raw}} \tag{11}$$

### *5.3 Finite Acceptance Correction to the Asymmetries*

Fig. 27 show the size of the finite acceptance correction to the asymmetry which is quite small.

## 6 Polarized Cross Section Difference Systematic

The systematic errors for the polarized cross section differences are evaluated from the unpolarized cross section and asymmetry errors as follows. The cross section difference is given by:

$$\Delta\sigma_{raw} = 2\sigma_T A_T \tag{12}$$

so,

$$\delta\Delta\sigma_{raw}^2 = \sqrt{(2A\delta\sigma_T)^2 + (2\sigma_T\delta A)^2} \tag{13}$$

where

$$\delta A = A\sqrt{\delta P_b^2 + \delta P_t^2} \tag{14}$$

and $\delta P_t = 0.04$ $\delta P_b = 0.03$, are the uncertainties on Target and Beam polarimetry respectively.

The elastic tail subtraction

$$\Delta\sigma_{raw} = \Delta\sigma_{raw} - \Delta\sigma_{elas} \tag{15}$$

leads to a further systematic uncertainty:

$$\delta\Delta\sigma^2 = \sqrt{(2A\delta\sigma_T)^2 + (2\sigma_T\delta A)^2 + \delta\Delta\sigma^2_{elas}} \tag{16}$$

where

$$\begin{aligned}
\delta\Delta\sigma_{elas} &= 0.10 \times \Delta\sigma_{elas}(\nu < 50MeV : 0.8GeV) \\
&= 0.20 \times \Delta\sigma_{elas}(\nu > 50MeV : 0.8GeV) \\
&= 0.10 \times \Delta\sigma_{elas}(\nu < 100MeV : 1.7GeV) \\
&= 0.20 \times \Delta\sigma_{elas}(\nu > 100MeV : 1.7GeV)
\end{aligned}$$

The elastic tail is insignificant for all other energies. There are several kinematics where the sequential spectrometer momentum settings do not overlap, and for which we must interpolate $\Delta\sigma$. In these regions, the systematic error is inflated by a factor of 1.3.

The uncertainty of the inelastic radiative corrections is accounted for as:

$$\delta\Delta\sigma^2_{born} = \sqrt{\delta\Delta\sigma^2 + (\delta RC * \Delta_{RC})^2} \tag{17}$$

where

$$\begin{aligned}
\delta RC &= 0.40(0.8 \text{ GeV}) \\
&= 0.20(\text{all other})
\end{aligned}$$

Here the uncertainty on the radiative corrections to the lowest incident energy has been doubled to account for the fact that the code must extrapolate into an unmeasured region to perform the radiative corrections. This error could be reduced by using the E97-110 data.

The spin structure functions $g_1$ and $g_2$ are related to the cross section differences as:

$$g_1(x,Q^2) = \frac{M_T Q^2}{2\alpha^2\hbar c}\frac{1}{2}\frac{y}{(1-y)(2-y)}\left(\Delta\sigma_{\parallel} + \tan\theta/2\Delta\sigma_{\perp}\right)$$

$$g_2(x,Q^2) = \frac{M_T Q^2}{2\alpha^2\hbar c}\frac{y}{4}\frac{y}{(1-y)(2-y)}\left[1/((1-y)\sin(\theta))(1+(1-y)\cos(\theta))\Delta\sigma_{\perp}\right]$$

or in simpler form as:

$$\begin{aligned}
g_1 &= C(A\Delta\sigma_{\parallel} + B\Delta\sigma_{\perp}) \\
g_2 &= D(E\Delta\sigma_{\parallel} + F\Delta\sigma_{\perp})
\end{aligned}$$

We use this to propogate the error to the structure functions.

$$\delta g_1 = \sqrt{C^2(A^2\delta\Delta\sigma_\parallel^2 + B^2\delta\Delta\sigma_\perp^2)}$$
$$\delta g_2 = \sqrt{D^2(E^2\delta\Delta\sigma_\parallel^2 + F^2\delta\Delta\sigma_\perp^2)}$$

And finally the sytematic errors are propogated to constant $Q^2$ along with the structure functions.

## 7 New Analysis Steps for 2007 and Further Comments

- Replaced all DIMENSION statements with REAL or INTEGER declarations. Previously, the DIMENSION statements bizarrely caused the RC factor to be 1 if ran on ifarml1. Modified dsig.f and sigtt.f to utilize IMPLICIT NONE and REAL8. Changed interpolation parameter DELTA=1.E-6. in radcor.f and dsig.f. It was previously 1.E-3 and 1.E-5 in radcor.f and dsig.f, which created some unphysical behaviour. In general, I attempted to make all codes compatible with simpler gnu compiler.

- Previously I made a $\sqrt{N}$ correction to the statistical error to account for the fact that the number of points interpolated to constant $Q^2$ differed from the number of measured data points. Although simple in concept, this proved very difficult to implement reliably, so I don't do it anymore. Now I apply no correction but just ensure that the number of interpolated points is approximately equal to the number of measured data points as shown in Fig 29. To check that the statistical errors are being propogated properly, I evaluated the structure function moments at the average $Q^2$ of the measured data and compared the uncertainty to the the final constant $Q^2$ results. The two agree favorably.

- Previously, I interpolated $\Delta\sigma$ to the leading edge of the first $\nu$-bin above threshold. This is incorrect. The value is now evaluated at the center of the bin, reflecting the histogram averaging of the data.

- Previously, the rebinning subroutine would include empty bins in the computation. This has unwanted effect near threshold: namely for the 862 MeV data, where we rebin from 1 MeV to 10 MeV bins, the first rebinned $\Delta\sigma$ point contained input from only two single 1 MeV bins, and had huge uncertainty. This propogated to unphysically large statistical uncertainty for the GDH sum due to the kinematic weighting of this bin.

- We insert an empty 'zero' bin just below threshold to stabilize the radiative corrections. The integrals show some sensitivity to the location of this zero. Previously, we placed it just fractionaly below threshold. Now we place the zero in a manner consistent with the data binning. That is, we place it at the 1st data point minus 1 bin.

- The collisional loss correction is applied only to the 862 MeV and 1717 MeV data set. These are the only data sets which utilize 1 MeV binning. The correction is assumed negligible for all other sets.

- I chose to use LCUT 13 for the unpolarized cross section which is actually smaller than the cut used in my thesis. This is due to the fact that this cut is insensitive to the finite acceptance correction. The statistical error on the cross section with LCUT 13 is still much less than the systematic error.

- We incorporated the radiative corrections of the unpolarized cross section into the polarized code to ensure that radiative corrections are applied consistently to the polarized and unpolarized data. Also, we now perform the RCs on a fit to the unpolarized data, just like we do for the polarized case.

- When filling in missing bins as a function of $\nu$ (for example, when there is no overlap between adjoining momentum settings), the code cleanXS.f increases the systematic of interpolated xs points by a factor 1.5 ( =50% ). The statistical error is interpolated directly.

- Previously, the born asymetry statistical errors could undergo a reduction when the radiative correction was applied. Now, I leave the statistical uncertainty unchanged by the radiative correction. This is strictly speaking incorrect, and the errors should reflect the fact that events migrate in/out of each bin with the RCs. However, the systematic error is deliberately large enough to absorb this effect.

- I modified the $\Delta\sigma$ fits to better track data, as shown in Fig. 28. This has a small but significant impact on the radiative corrections, especially in the quasielastic region for the 1.7 GeV data set. Also, modified the fitting procedure to base fits on the total error of the data, not just the statistical error.

- I now interpolate only $g_1$ and $g_2$ to constant $Q^2$, and then form all other physics quantities from these structure functions. Previously, I separately interpolated $g_1$, $g_2$, $\sigma_{TT}$, $\sigma_{LT}$ and the integrand of $d_2$.

- The interpolation to constant $Q^2$ assumes good W-scaling, except for the low energy (high nucleon momentum) side of the quasielastic peak. To perform the $Q^2$-interpolation in this region, I fit the Q.E. peak position of the unpolarized cross sections and assigned this a value Z=1 as reflected in Fig. 29. Then I assigned Z=0 to the 2 body breakup threshold. For all W in this region a value of Z is assigned based on a linear interpolation from Z=0 to Z=1. This value of Z is then used to perform the $Q^2$ interpolation. In the previous analysis, I utilized a more arbitrarily

defined Z variable, and used Z to perform all $Q^2$ interpolations whenever the invariant mass was less than the pion production threshold.

- As described in my thesis, I performed the $Q^2$ interpolation by first subtracting out an assumed exponential background. In fact, the data behaves exponentially only in the regions immediately surrounding the quasielastic peak and resonances. In other regions, exponential behaviour is in fact a poor description of the data. Now, before subtracting out the exponential, I test to ensure that the data is atleast monotonically increasing or decreasing. The solid symbols in Fig. 30 reflect where this criteria holds and the exponential background subtraction succeeded. If the monotonic condition is not satisfied, no background is subtracted out prior to interpolation.

- After the exponential background is subtracted, I look at several different orders of interpolation in order to guage the systematic uncertainty. For the $Q^2$ interpolation, I compare linear, quadratic, and cubic, while the W interpolation compares linear, quadratic results, for total of 6 different possibilities. The final structure functions represent the average of all these results, and the systematic is evaluated as the standard deviation (using N-1). After the interpolation, the fitted background is added back in.

- I changed the code sigtt.f so that in the few regions where W-extrapolation is needed, the code now uses fits to the data instead of the raw data itself. (In the notation of the code, ISTAGE=3 values are substituted for ISTAGE=4 values whenever a W-extrapolation is performed.) The statistical error on these fitted values is taken as a conservative 10%.

- The code values for the neutron and proton elastic contribution to the GDH Sum ( GDH_N_EL and GDH_P_EL) were previously incorrect. The only impacts are on the neutron GDH results when elastic is included, or in the 'supermaid' results when not using scopetta's PWIA.

- It is best not to use the '.cln' option for asymmetries as this removes way too many runs.

- The transverse-transverse cross section can be expressed in terms of $g_1$ and $g_2$: $\sigma'_{TT} = -\frac{4\pi^2\alpha}{mK}\left(g_1 - \gamma^2 g_2\right)$. It is interesting to note that because of the kinematic factors, $g_2$ dominates $\sigma_{TT}$ in the Q.E. region for the lowest $Q^2$ data.

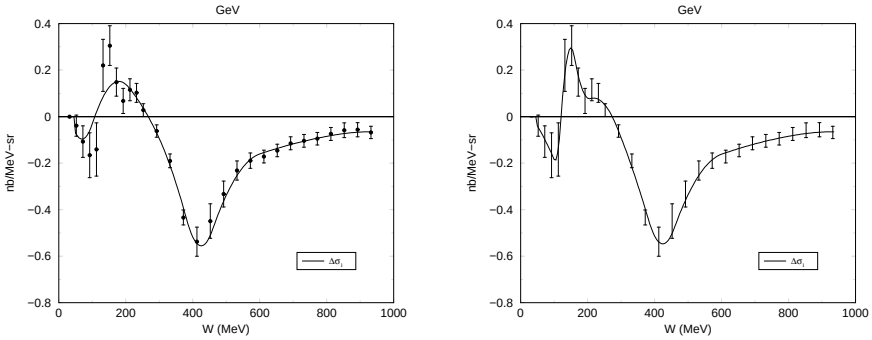


Figure 28: Fit used for radiative corrections. **Left:** Old fit **Right:** New fit

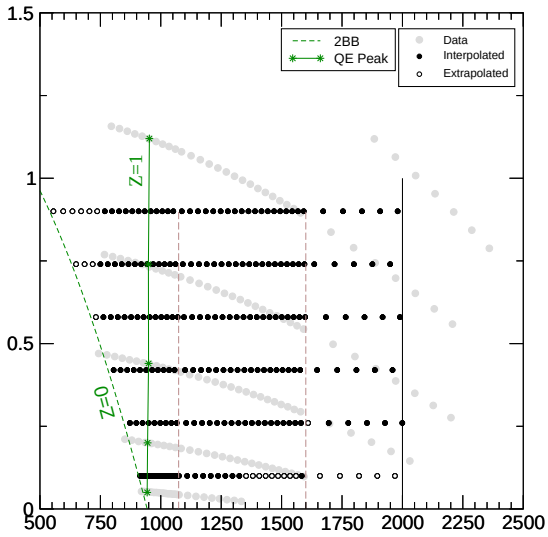


Figure 29: Gray symbols represent the measured data points. Filled black symbols are interpolated to constant $Q^2$. Open symbols represent extrapolation.

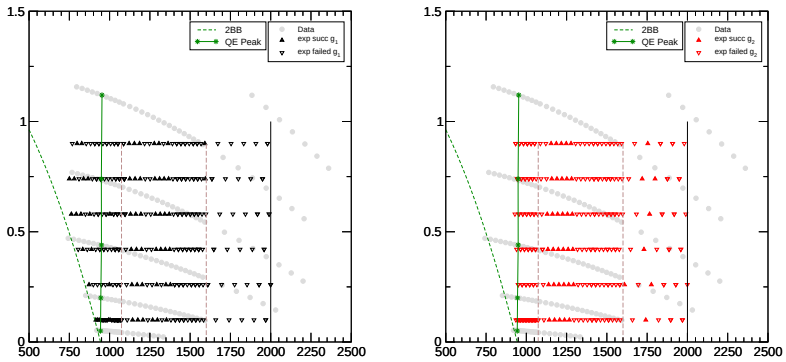


Figure 30: The solid symbols reflect where the exponential fit succeeded for $g_1$ and $g_2$.

| $\mathbf{E_0(GeV)}$ | **0.8** | **1.7** | **2.5** | **3.3** | **4.3** | **5.1** |
|---|---|---|---|---|---|---|
| C | -3.81108 | -2.60736 | -0.946233 | -0.60113 | -0.455952 | -0.377751 |
| $\alpha$ | 0.986584 | 0.97756 | 0.946493 | 0.922936 | 0.904321 | 0.889245 |
| $\beta$ | 3.72122 | 2.55588 | 0.853467 | 0.48789 | 0.330621 | 0.244916 |

Table 5: Values obtained for the fit form of Eq. 18.

## 8 DIS contribution to Integral

The DIS contribution to the $^3$He GDH Integral and $\Gamma_1$ was estimated using the Bianchi and Thomas parameterization of $\sigma_{TT}$ for $2 < W < \sqrt{1000}$ GeV. We estimated the remaining contribution to the integral for $x \to 0$ by fitting the DIS Bianchi and Thomas results to a Regge type form:

$$g_1 = Cx^{\alpha-1} + \beta \tag{18}$$

The results can be found in Table 5. The contribution from this region to the integral amounted to 1.3 - 2.5% of the $2 < W < \sqrt{1000}$ GeV integral and is negligible compared to the systematic uncertainty of our DIS estimate.

## 9 References


1. K. Slifer Thesis.
2. N. Liyanage technote.
3. K. Slifer. E94010 codes.
4. A. Deur Elastic note.
5. Mo and Tsai, Stein et al.
6. Polrad.
7. NIST STAR